European Conference on Computational Fluid Dynamics
ECCOMAS CFD 2006
P. Wesseling, E. Oñate and J. Périaux (Eds)

COMPRESSIBLE SIMULATION OF HIGH-SPEED HYDRODYNAMICS WITH PHASE CHANGE

Steffen J. Schmidt*, Ismail H. Sezal and Günter H. Schnerr

*Technische Universität München, Faculty MW
Boltzmannstraße 15, D - 85748 Garching , Germany
e-mail: schmidt@flm.mw.tum.de
web page: http://www.lhm.mw.tu-muenchen.de/gd/

Key words: Cavitation, Riemann solvers, Hydrodynamics, Injection nozzles

Abstract. *The present paper focuses on a numerical approach based on the Riemann problem to simulate liquid flows with phase changes. Thereby, the flow properties include velocities from $\mathcal{O}(1)$ m/s to $\mathcal{O}(100)$ m/s and pressures from $p \approx 0$ bar to $\mathcal{O}(1000)$ bar. The thermal and caloric behavior of liquid and vapor is described by suitable equations of state that keep the considered governing equations hyperbolic in time. This enables us to study single-phase as well as two-phase wave propagation phenomena, which can have strong effects on the performance of dynamic systems, e.g. on high-speed hydrodynamics in injection nozzles or in high pressure valves. Our physical model is based on the assumption that the two-phase regime can be described as a homogeneous mixture that remains in thermodynamic and mechanical equilibrium. This model provides a macroscopic description of the phase change and is independent of empirical parameters. Subsequent to the description of the mathematical model and the numerical method, computations are carried out to demonstrate the accuracy and applicability of the numerical scheme to liquid flows for a large variety of industrial problems. Finally, the simulation results of the time-dependent cavitating flow through a 3-D injection nozzle will be presented.*

1 INTRODUCTION

Liquid flows at low or at least moderate Mach numbers are usually described as being incompressible. This simplification is justified by the observation that the density change along a particle path is almost zero as long as no phase change occurs. As a result, the continuity equation reduces to a kinematic constraint on the velocity field. Furthermore, the pressure is no longer a thermodynamic state variable and thus one has to calculate it from the known velocity field by a Poisson type equation. An important consequence of this formulation is the loss of hyperbolicity of the time-dependent convective flow equations, which means that the mathematical model does no longer describe wave motion with finite propagation speeds. In the case of subsonic steady-state solutions this treatment

gives satisfactory results. For unsteady flow patterns the elliptic pressure treatment can lead to completely wrong predictions, for example when calculating the pressure raise in a water hammer. Especially when dynamic systems such as high-speed valves or injection systems are considered, the wave propagation and thus the compressibility has to be taken into account. Most of the work done so far does consider only 1-D geometries[1]. Even if there is no external force present that introduces pressure waves to the flow field, strong compressibility effects can be observed when the liquid undergoes phase change. We will exclusively focus on phase change phenomena caused by a local pressure drop below the temperature-dependent saturation pressure - cavitation - , or if vapor is already present and the pressure rises above its saturation value - condensation. Both effects can be a consequence of acceleration or deceleration of the flow due to geometry properties as well as due to rarefaction or shock waves. The description of microscopic details of the phase change is beyond the scope of this investigation but there has been numerous research on this subject[2,3]. Instead we will follow the assumption that a given fluid volume can be represented by either a pure phase or by a homogeneous saturated mixture[4]. In the case of a mixture region we define macroscopic quantities. This can be achieved by the assumption that the flow particles undergo unconstrained thermodynamic equilibrium. Moreover, the equilibrium assumption enables us to define an equilibrium speed of sound c, which will be used to calculate the wave propagation in the two-phase mixture as well as in single phase regions.

2 GOVERNING EQUATIONS

As we are mainly interested in the wave dynamics of convective high-speed hydrodynamics, we base our mathematical model on the conservation laws of mass, momentum and energy and neglect viscous effects. The saturated mixture quantities are then defined as convex combinations of mass or volume fractions of the pure quantities. For liquid states we use the index l and for vapor states the index v is taken. Quantities without index represent either vapor-liquid equilibrium properties in the two-phase region or pure substance properties in single-phase regions. We further use the notations:

$$\begin{aligned} \alpha &:= \frac{V_v}{V_v + V_l} && \text{volume fraction of vapor} \\ \mu &:= \frac{\rho_v V_v}{\rho_v V_v + \rho_l V_l} && \text{mass fraction of vapor.} \end{aligned} \tag{1}$$

Mass and volume fractions fulfill the relations

$$0 \leq \alpha \leq 1 \quad \text{and} \quad 0 \leq \mu \leq 1. \tag{2}$$

The mixture density and the mixture internal energy can then be defined by

$$\begin{array}{rcccccl} \rho & = & \alpha\rho_v & + & (1-\alpha)\rho_l & & \\ \rho e & = & \alpha\rho_v e_v & + & (1-\alpha)\rho_l e_l & = & \rho\big\{\mu e_v + (1-\mu)e_l\big\}. \end{array} \tag{3}$$

By interpreting the mixture quantities $(\rho, \rho\vec{\mathbf{v}}, \rho E)$ as densities with respect to the Lebesgue measure we find formally the same set of equations as for single phase flows:

$$\begin{array}{rcccl} \partial_t\, \rho & + & \mathrm{div}(\rho\vec{\mathbf{v}}) & = & 0 \\ \partial_t(\rho\vec{\mathbf{v}}) & + & \mathrm{div}(\rho\vec{\mathbf{v}}\otimes\vec{\mathbf{v}} + p\underline{\mathbf{I}}) & = & \vec{0} \\ \partial_t(\rho E) & + & \mathrm{div}(\rho H\vec{\mathbf{v}}) & = & 0. \end{array} \tag{4}$$

Here, $\vec{\mathbf{v}} \in \mathbb{R}^3$ and $\underline{\mathbf{I}} = \delta_{ij}$. The total enthalpy H is given by:

$$H = E + \frac{p}{\rho} = e + \frac{|\vec{\mathbf{v}}|^2}{2} + \frac{p}{\rho}. \tag{5}$$

Furthermore, constitutive relations for the remaining quantities are needed. At this point we assume relations for pressure and internal energy to be given in the form

$$p = p(\rho, e) \quad \text{and} \quad T = T(\rho, e). \tag{6}$$

By writing the system (1) in quasi-linear form and calculating the eigenvalues in unit direction $\vec{\mathbf{n}}$ one obtains[5]:

$$\vec{\mathbf{v}}\cdot\vec{\mathbf{n}} - c,\ \vec{\mathbf{v}}\cdot\vec{\mathbf{n}},\ \vec{\mathbf{v}}\cdot\vec{\mathbf{n}},\ \vec{\mathbf{v}}\cdot\vec{\mathbf{n}},\ \vec{\mathbf{v}}\cdot\vec{\mathbf{n}} + c \tag{7}$$

where c^2 is defined by

$$c^2 = \left.\frac{\partial p}{\partial \rho}\right|_s = \left.\frac{\partial p}{\partial \rho}\right|_e + \frac{p}{\rho^2}\left.\frac{\partial p}{\partial e}\right|_\rho. \tag{8}$$

The Euler system (4) is hyperbolic if and only if $0 < c^2 < \infty$. Then the quantity c is called equilibrium speed of sound[6].

3 EQUATIONS OF STATE (EOS) FOR LIQUID, VAPOR AND SATURATED MIXTURE

In this section we give an example for the constitutive relations (6), which are suitable to describe the properties of water and water vapor for thermodynamic subcritical

conditions occurring in a large range of practical applications. Note that the general numerical method is not restricted to this special choice and hence, the use of problem-suited relations is possible.

3.1 EOS for liquid water

One often used relation for the properties of liquid water is the Tamman EOS or sometimes called Stiffened equation of state[7]. This EOS is well-designed for very high pressures and its evaluation is extremely fast. Unfortunately, for the considered pressure regime from nearly 0 bar up to 1000 bar the Tamman EOS is not suitable. Another well known relation is given by Tait's law:

$$\frac{p+B}{p_{ref}+B} = \left(\frac{\rho}{\rho_{ref}}\right)^N. \tag{9}$$

This equation is often used to describe isentropic variations and a thermally consistent description for the corresponding internal energy could be of the form:

$$e_l = C_{v_l}(T - T_{ref}) + e_{l_{ref}}. \tag{10}$$

In EOS (9) and (10) the reference values $(\cdot)_{ref}$, the "bulk coefficient" B, the "adiabatic exponent" N and the specific heat at constant specific volume C_{v_l} are assumed to be constants. The accuracy of the pressure law (9) can be increased by the use of temperature-dependent saturation values instead of constants[4]. We then obtain the modified Tait law:

$$\frac{p+B}{p_{sat}(T)+B} = \left(\frac{\rho}{\rho_{l,sat}(T)}\right)^N. \tag{11}$$

Equation (11) can be interpreted as a set of self similar curves starting from saturation values and then following Tait's law. Again, B and N are assumed to be constant. Unfortunately, the modified Tait equation together with formulation (10) does not fulfill Maxwell's relations. Nevertheless it gives an useful description not only for water but for a large range of materials[8,9]. It should be further pointed out that the resulting errors by checking the compatibility relations are relative small and hence, we suggest that the modified Tait law (11) together with (10) can be an appropriate set of constitutive relations for liquid flows. As the saturation properties are typically given by high-order non-linear functions (e.g. Oldenburg polynomials[10] for water and water vapor), the evaluation procedure is further simplified by approximating the saturation functions by problem specific lower order relations.
The speed of sound c_l for liquids is then found by applying (8) on (10) and (11). The obtained values do in general agree well with the measurement data[11], but relative errors up to three percent are possible.
All calculations in section 5 are performed with the same reference values, which can be found in the appendix.

3.2 EOS for water vapor

In comparison to liquids, the thermodynamics of ordinary gases at moderate conditions can be modeled in a more compact way. The simplest but still appropriate formulation is given by the ideal gas law:

$$\begin{aligned} p &= \rho_v R T \\ e_v &= C_{v_v}(T - T_{ref}) + e_{l_{ref}} + L_{v_{ref}}. \end{aligned} \tag{12}$$

For the sound speed c_v in pure vapor the well known relation $c = \sqrt{\kappa R T}$ is applied. Again, the used constants are given in the appendix.

3.3 EOS for saturated two phase mixture

The assumption of thermodynamic equilibrium enables us to define mixture states by the following conditions:

$$\begin{aligned} \rho &= \alpha\rho_{v_{sat}}(T) + (1-\alpha)\rho_{l_{sat}}(T) \\ \rho e &= \alpha\rho_{v_{sat}}(T)e_v(T) + (1-\alpha)\rho_{l_{sat}}(T)e_l(T) \\ p &= p_{sat}(T). \end{aligned} \tag{13}$$

The temperature-dependent saturation densities of water and vapor can again be approximated by exponential functions (appendix). Note that by solving the first equation for the volume fraction α and applying the result to the second equation we find:

$$\rho e = \frac{\rho - \rho_{l_{sat}}(T)}{\rho_{v_{sat}}(T) - \rho_{l_{sat}}(T)} \Big\{ \rho_{v_{sat}}(T)e_v(T) - \rho_{l_{sat}}(T)e_l(T) \Big\} + \rho_{l_{sat}}(T)e_l(T). \tag{14}$$

This is a single nonlinear equation for the unknown temperature T, which can be solved via appropriate numerical methods. In our case we have found a contradictive formulation, and by applying Banach's theorem we obtained a simple fixpoint scheme which has proven to be at least 3 to 4 times faster then our previously used Newton method. If the temperature is found, the first equation gives the volume fraction in a self-consistent way and the calculation of the saturation pressure is easily done.
The calculation of the mixture speed of sound c can be simplified by the commonly used formula[1,2] given by Wallis[12]. This leads to the relation:

$$\frac{1}{\rho \cdot c^2} = \frac{\alpha}{\rho_{v,sat} \cdot c_v^2} + \frac{1-\alpha}{\rho_{l,sat} \cdot c_l^2}. \tag{15}$$

Evaluating this expression for saturation values, a very strong dependence on the vapor

fraction α can be observed. The quantitative behavior for $T = 293\ K$ is demonstrated in Fig. 1 (left). Note that the sonic speed decreases from $\mathcal{O}(1000)\ m/s$ to $\mathcal{O}(1)\ m/s$. Even

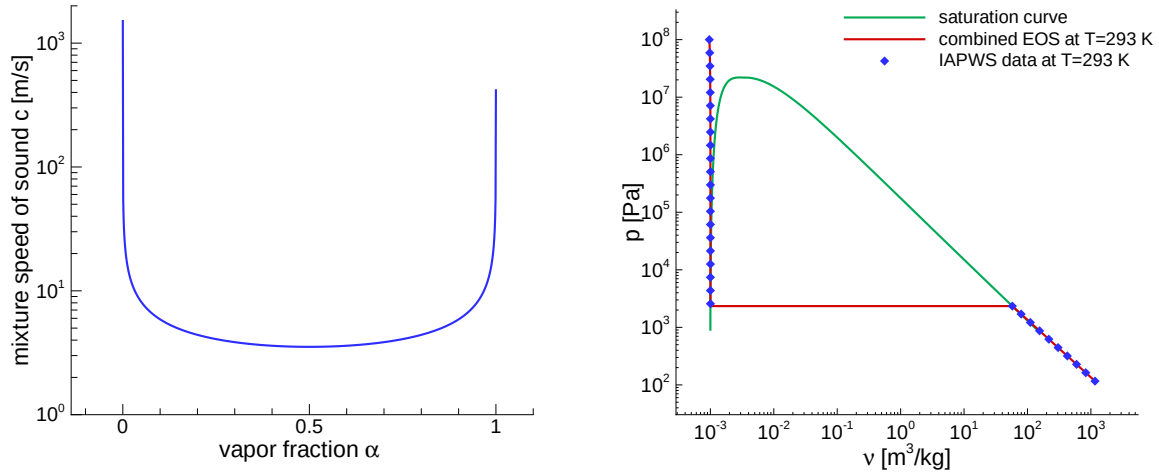

Figure 1: Speed of sound c for a two phase mixture in logarithmic scale (left) and combined EOS at T=293 K and IAPWS data[13] (right)

for very tiny mass and volume fractions an enormous reduction of the speed of sound is observable. This fact was experimentally used to generate hypersonic flow fields at relative low convective speeds[14].

3.4 Combined EOS for liquid flows with phase change

Connecting the above defined equations of state leads to a complete description of the properties of liquid and vapor. It should be pointed out that more accurate equations are known[15]. The advantages of the procedure given above are its applicability to fluids other then water and its high numerical efficiency. A comparison of the combined EOS with IAPWS measurement data[13] at a temperature $T = 293\ K$ is given in Fig. 1 (right).

4 NUMERICAL METHOD

The formulation of the governing equations as conservative hyperbolic system motivates the use of specially adapted solution strategies, such as the Godunov approach[16]. Although the Riemann problem is completely understood for 1-D ideal gas flows, the extension to multidimensions and arbitrary equations of state is still somehow empirical. Nevertheless, most of the results obtained by Godunov-type schemes are convincing and especially the sharp wave capturing ability is up to now not reached by other methods. A general Riemann problem description with special remark on ideal gases is given by

Toro[17]. The Riemann problem for water and the interesting case of Riemann problems for water/gas interfaces are solved for special equations of state[7,18]. General remarks on real material flows can be found in the literature[19]. In the last few years, the density-based solution procedures for the Cauchy problem of fluid dynamics have reached enormous interest and successful and sophisticated numerical codes have been developed[20]. While being well-designed for time-dependent wave propagation phenomena, it was found out[21] that the calculation of steady-state flows at sufficiently low Mach numbers cannot be done without modifying the density-based schemes. The introduction of asymptotic expansions in natural powers of the Mach number show that the numerical problems arising for M sufficiently small are due to wrong calculations in the pressure field[22]. To solve these drawbacks, a modification of the numerical dissipation was found to be successful[23]. The next subsections are therefore organized as follows: First, an approximate solution of the Riemann problem is given and the influences of the fluid properties on the accuracy of a numerical simulation are briefly discussed. As a main result, the calculation of the pressure flux may need some modifications to ensure accurate steady state solutions. Taking these modifications into account, a hybrid solution approach is given in subsection 4.2.

4.1 Accuracy of well-known Riemann solvers

Before we give a brief description of the numerical difficulties to solve compressible liquid flows we introduce further quantities and notations. Therefore a schematic sketch of the Riemann problem and the arising quantities is given in Fig. 2. The quantities on the

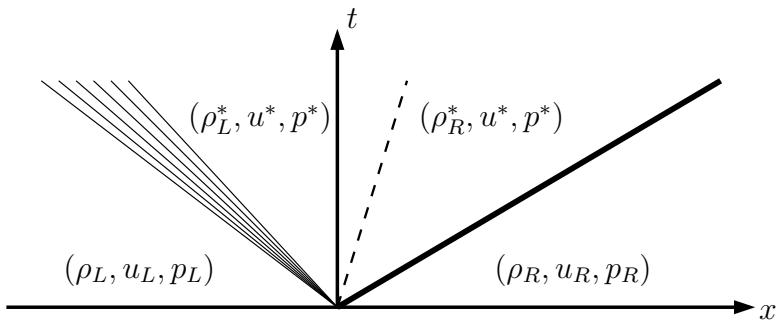

Figure 2: Schematic 1-D Riemann problem

very left ("L") and on the very right sides ("R") are the known integral averages from the last timestep. To calculate the fluxes over the cell faces, the star conditions $(\rho_L^*, \rho_R^*, u^*, p^*)$ are required. By assuming that the two outer states are close to some averages, a local linearisation around that averages could be performed and an approximate solution is

obtainable by applying Rankine-Hugoniot conditions across each wave:

$$\begin{aligned} u^* &= \frac{u_L + u_R}{2} + \frac{p_L - p_R}{2\bar{\rho}\bar{c}} \qquad & p^* &= \frac{p_L + p_R}{2} + \frac{\bar{\rho}\bar{c}(u_L - u_R)}{2} \\ \rho_L^* &= \rho_L + \frac{\bar{\rho}(u_L - u^*)}{\bar{c}} \qquad & \rho_R^* &= \rho_R + \frac{\bar{\rho}(u^* - u_R)}{\bar{c}} \end{aligned} \tag{16}$$

Note that the linearisation replaces the waves in the genuinely non-linear fields by jump discontinuities independently of the specific wave types. The barred variables $\bar{\rho}, \bar{c}$ could be specified as arithmetic means of left and right-sided values. Although more sophisticated approximations for the star conditions are known[17], the general properties of the resulting fluxes are quite similar to the one given above. Especially the behavior of the second equation should be briefly discussed: Therefore, we consider an inviscid steady water flow through a one-dimensional duct at a (nearly) constant temperature of 320 Kelvin and a constant total pressure of 1.125 bar. The velocity is assumed to accelerate from $5m/s$ at position x_1 to 15 m/s at position x_2. For these conditions, the steady density and sonic speed distributions will be to best approximation constants, say $\rho \cong 1000\ kg/m^3$ and $c \cong 1540\ m/s$. The static pressure drop can then be calculated from the Bernoulli equation and one obtains: $p(x_1) = 1\ bar$ and $p(x_2) = 0\ bar$. Note that the static pressure and the velocity both vary in the order of their "farfield values" at position x_1. Although the Mach number M of this problem is strictly smaller then 0.01, we are not allowed use the asymptotic techniques developed for low Mach number flows, because the leading-order variations do not permit the introduction of M-expansions[22]. In the context of a finite volume approach all quantities are given by integral averages. Assume the discretization leads to the following left- and right-sided values:

$$\begin{aligned} &u_L = 5\ m/s, && u_R = 5.13\ m/s, \\ &p_L = 1\ bar, && p_R = 0.993\ bar, \\ &\rho_L = 1000\ kg/m^3, && \rho_R = \rho_L - \varepsilon \quad (\varepsilon \ll 1). \end{aligned} \tag{17}$$

Evaluating the expressions in (16) does then give the conditions

$$u^* \approx 5.056\ m/s, \quad p^* \approx 0\ bar. \tag{18}$$

On the one hand both values can be verified to be quite accurate solutions of the Riemann problem for the given left and right sides. On the other hand the obtained pressure value indicates the difficulty to calculate the numerical flux for a smooth water flow. The calculated interface pressure p^* is extremely sensitive even to small "discrete jumps" in the velocity field. An explanation for this behavior could be obtained by the following observation: For nearly constant density and sonic speed the numerical approximation of the pressure $p_{L,R}$ at the cell interface is given by the p^* relation in (16):

$$p_{L,R} = \frac{p_L + p_R}{2} + \Delta x \rho c \frac{(u_L - u_R)}{2\Delta x} = \frac{p_L + p_R}{2} - \Delta x \rho c \frac{u'(\xi)}{2} \tag{19}$$

One can identify the product ρc as a scaling factor on the mesh dependent dissipation term $\Delta x u'(\xi)$. As a consequence, the use of the quantities arising from the Riemann problem to calculate the fluxes over the cell faces (as commonly done in the approximate Godunov approach) results in a scheme with a truncation error of $\mathcal{O}(\rho c \cdot \Delta x)$. A comparison of air and water at standard conditions leads to:

$$(\rho c)_{air} = \mathcal{O}(10^2) \quad \text{and} \quad (\rho c)_{water} = \mathcal{O}(10^6) \tag{20}$$

From equation (20) it can be concluded that the calculation of a steady water flow may require a much finer grid than a comparable air flow. Unfortunately, this is a consequence of the discretization and not part of flow physics, as the velocity jumps are - for the suggested smooth flow - not physically present. Keeping this in mind we can determine possible ways to obtain accurate solutions for steady and unsteady liquid flow problems: Fine grids, high-order reconstructions and/or a modification of the pressure flux calculation. The first two suggestions are in general limited in their efficiency and do not seem to be sufficient to obtain accurate steady-state results on typical 2-D and 3-D grids. This will be demonstrated in section 5.3 for a 2-D single-phase calculation.

4.2 Hybrid solver based on the Riemann problem and flux splitting

In order to study the behavior of well known flux functions we have applied the schemes of ROE, HLL and HLLC, as well as the Rusanov scheme and two simple linearized schemes on steady and unsteady water flow problems[17]. All schemes failed to give accurate steady-state solutions for typical 2-D and 3-D nozzle flows, but they performed excellent or at least satisfactory on shock tube problems. As supposed in the previous section, the steady-state solutions indicated a strongly dissipative behavior. Contrary to the mentioned flux functions, the AUSM+ scheme[24] performed quite well for $t \to \infty$. For shock tube calculations the scheme produced acceptable results but the mass flow was not as accurate as the one predicted by the ROE or HLLC fluxes. Comparing the pressure flux calculation in the AUSM type methods[24,25] with those methods that are directly related to the Riemann problem, one can figure out that the AUSM pressure splitting contains a significantly lower diffusion term. For the nozzle flow problem stated above the interface pressure calculated by the AUSM scheme is about 0.9 *bar*, which seems more reasonable than the result given in equation (18). We therefore tried to combine the AUSM flux with the HLLC flux to obtain a scheme[26] that is able to handle problems containing nearly steady regions as well as time dependent wave phenomena. Therefore, we follow the general philosophy of the AUSM type methods and divide the conservative Euler fluxes $F(Q)$ into a "convective component" and a "pressure part". This leads to the formula:

$$F(Q) = \begin{pmatrix} \rho u \\ \rho u u + p \\ \rho u v \\ \rho u w \\ \rho u H \end{pmatrix} = (\rho u) \cdot \begin{pmatrix} 1 \\ u \\ v \\ w \\ H \end{pmatrix} + \begin{pmatrix} 0 \\ p \\ 0 \\ 0 \\ 0 \end{pmatrix} = \dot{m} \cdot F_{conv} + F_{pres} \tag{21}$$

The mass flux $\dot{m} := (\rho u)$ is a common scalar for the convective flux. Instead of approximating $\dot{m}$ via polynomials (as done in the original AUSM methods) we use the HLLC mass flux[17]. For the schematic sketch given in Fig. 2 the mass flux reads then:

$$\dot{m} := (\rho_L^* u^*) \tag{22}$$

The convective vector F_{conv} is build up by pure left side states for positive mass flow and otherwise by right side values. This is again a common part of AUSM. To determine the pressure flux F_{pres} we apply the AUSM pressure splitting without additional modifications. The resulting interface pressure $p_{L,R}$ can be written as:

$$p_{L,R} := \mathcal{P}_5^+(u_L/c_L) \cdot p_L + \mathcal{P}_5^-(u_R/c_R) \cdot p_R \tag{23}$$

A very detailed description of the AUSM scheme including the full presentation of the polynomials $\mathcal{P}_5^{\pm}$ for the pressure splitting can be found in the literature[24].

4.3 Higher-order spatial reconstructions

The finite volume framework leads to a method of lines type approach where the spatial discretization can be selected independent of the time marching scheme. Although the straight forward extension of the TVD theory to multi-dimensions has proven to be not successful in a rigorous mathematical sense[27], the so called MUSCL-type reconstructions have been successfully used for many years. We apply the reconstruction procedures in a coordinate-wise manner on the variables ρ, u, v, w, e and select the type of limiting depending on the flow properties. For cavitating flows a positivity preserving reconstruction is needed for the density, such as the MinMod limiter[27]. The velocity field is recovered by a WENO-3 reconstruction[28] and for the internal energy we apply the VanLeer limiter[5].

4.4 Temporal integration

As the resolution of pressure waves requires a very small time step we use explicit time marching schemes only. We have tested a second order TVD-Runge-Kutta method[29] as well as a non-TVD four stage second order low storage RK scheme[5]. Both worked stable and accurate for all our numerical examples. It follows from the theory[29] that the CFL number for the TVD-RK has to be taken very small (< 0.3) to keep the scheme in the TVD region. The four stage RK allows a $CFL \approx 1.5$ and although it does not ensure TVD we did not observe overshoots for the simulations done jet.

5 NUMERICAL EXAMPLES

In the following section we validate the numerical scheme for 1-D and 2-D test cases and apply it then to a 3-D geometry. If possible, the obtained solutions will be compared with analytical results.

5.1 1-D single phase time-dependent test case

In order to verify the stability and the wave capturing ability of our method we start with a well-known Joukovski-Shock or water hammer problem, which is actually an ordinary moving normal shock. Thereby, a stationary water flow through a pipe with constant area and the constant conditions $\rho = \rho(p_\infty, T_\infty)$, $u = u_\infty > 0$, $p = p_\infty$ and $T = T_\infty$ is considered. At time $t = t_c$ the outflow boundary is entirely closed and a pressure rise at the wall instantaneously occurs. This (weak) shock wave then travels in opposite direction to the flow. Again, the pressure jump can be approximated by solving the generalized Riemann invariant across the wave

$$dp + \rho c du = 0 \quad \text{across} \quad \dot{x} = u - c. \tag{24}$$

By evaluating the product ρc at the foot of the characteristic one obtains:

$$p^* = p_\infty + \rho_\infty c_\infty u_\infty. \tag{25}$$

Using the experimental data from[11] we find for water at conditions $T_\infty = 319.0\ K$ and $p_\infty = 0.9\ bar$ the corresponding density $\rho_\infty = 989.86\ kg/m^3$ and the corresponding sonic speed $c_\infty = 1537.16\ m/s$. Taking $u_\infty = 1.0\ m/s$ and evaluating (25) for these conditions gives

$$p^* = 16.12\ bar. \tag{26}$$

We now perform a numerical simulation by using p_∞, T_∞ and u_∞ as stated above. The corresponding density and sonic speed follow thereby from the equation of state. First we find

$$\rho_{\infty,eos} = 989.84\ kg/m^3 \quad \text{and} \quad c_{\infty,eos} = 1544.14\ m/s. \tag{27}$$

The relative errors in density and sonic speed are $\Delta\rho/\rho_\infty = 2 \cdot 10^{-5}$ and $\Delta c/c_\infty = 4 \cdot 10^{-3}$. The calculated pressure after the shock gives $p^*_{num} = 16.20\ bar$. Taking the analytical estimate (26) as reference we find the relative error $\Delta p^*/p^* = 5 \cdot 10^{-3}$.

Remark 1: Calculating the Joukovski-Shock by integrating characteristic compatibility relations across the shock (equations 24, 25) results in an underestimation of the pressure jump. It is possible that the numerical result, which predicts a shock Mach number of $M_S \approx 1.0008$, is closer to the true solution then the analytical estimate.

Remark 2: Contrary to steady subsonic flow patterns, the water hammer can not be

calculated with an incompressible formulation. The divergence-free condition in incompressible formulations does not permit the formation of the necessary pressure wave and instead of the true time-dependent behavior the velocity in the whole pipe will be set to zero after the first time step. From a physical point of view, this could be interpreted as an infinitely fast signal speed, which is a general model error of incompressible formulations.

5.2 1-D two phase time-dependent test case

In this subsection we use the combined EOS and decrease the density below the saturation density of pure liquid by enforcing two symmetric expansion waves. The domain is given by a 1-D constant area tube with length 1 m. At time $t = 0$ s the whole tube is filled with water at a temperature $T = 303.15$ K and a pressure $p = 0.9$ bar. The velocity field is assumed to jump at $x = 0.5$ m from $u_L = -10$ m/s to $u_R = 10$ m/s. These conditions enforce the phase change to occur. In Fig. 3 the resulting flow features at time $t = 1.5 \cdot 10^{-4}$ s are shown. The domain was divided into 300 equally spaced cells and the time integration was performed with the LS-RK 4 at $CFL = 1.5$.

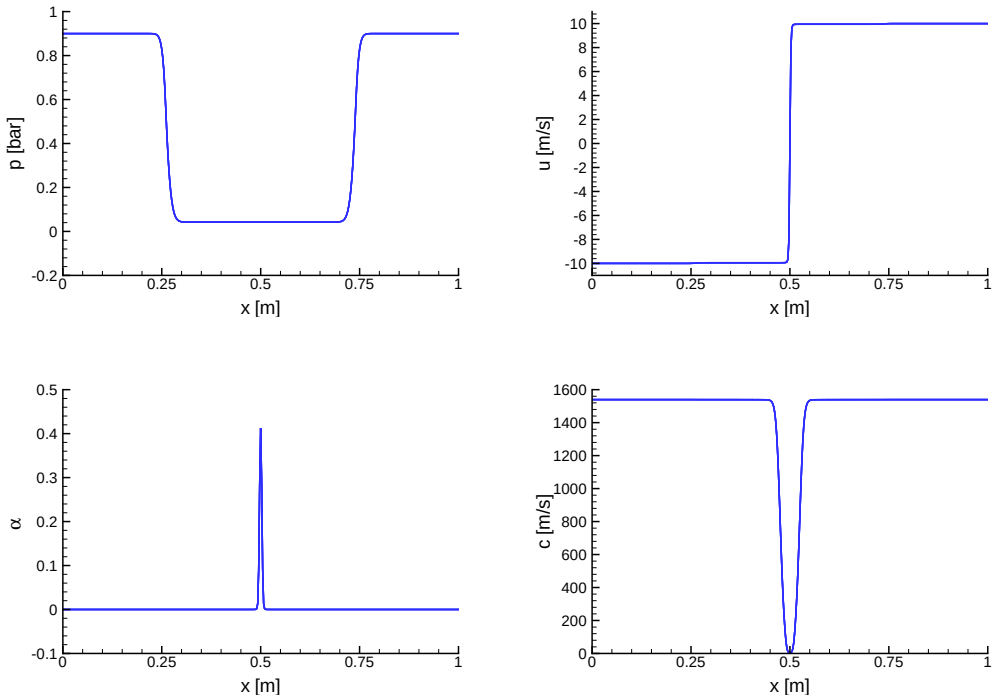

Figure 3: Flow quantities at time $t = 1.5 \cdot 10^{-4}$ s for the 1-D symmetric rarefaction problem.

5.3 2-D Single Phase Steady-states

We now compare our solution strategy with the well-known HLLC approach[7,17]. Therefore, we define a 2-D geometry typical for injection nozzles and search for the enforced single phase steady-state solution. This means that we do not allow the liquid to undergo a phase change by using the pure liquid EOS even if the density falls below its saturation value. The same simulation was performed with higher pressure fields, but the qualitative behavior was not affected. The geometry and the boundary conditions are given in Fig. 4. The spatial discretizations are the first order schemes (without any reconstruction)

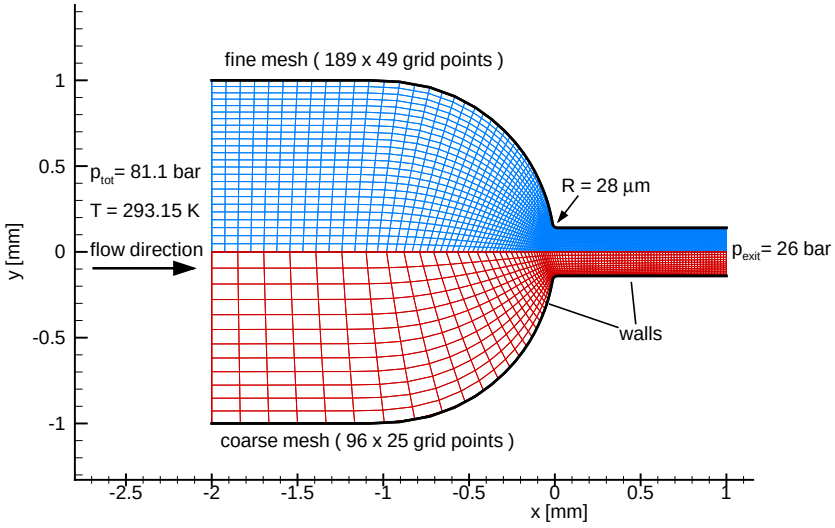

Figure 4: 2-D plane nozzle geometry, fine grid (top half), coarse grid (bottom half) and boundary definitions

and the quadratic interpolation of cell averages without limiters. The later one corresponds to a third order accurate formulation on equally spaced one dimensional grids[5]. For the time-marching the four stage RK scheme is applied and all solutions converged at least seven orders in magnitude measured in the common L_2-Norm of the conserved quantities. The boundary conditions are subsonic inlet, subsonic outlet and adiabatic inviscid walls. At the inlet we fix total pressure, static temperature and the direction of the velocity. At the outlet, the static pressure is specified and all remaining quantities are taken from inside. All boundaries are defined by ghost cells and hence, the treatment of a boundary cell is equivalent to the treatment of the interior domain. The grids for the full symmetric nozzle consist of 96 x 25 points (coarse grid) and 189 x 49 points (fine grid),

both with finer treatment of the region where the small corner like radius $R = 28\ \mu m$ will produce large gradients. For presentation purposes we show one half of the nozzle for each solver. The top half of each nozzle picture shows the result obtained with HLLC and the bottom shows the result of the Hybrid scheme. To verify the obtained solutions

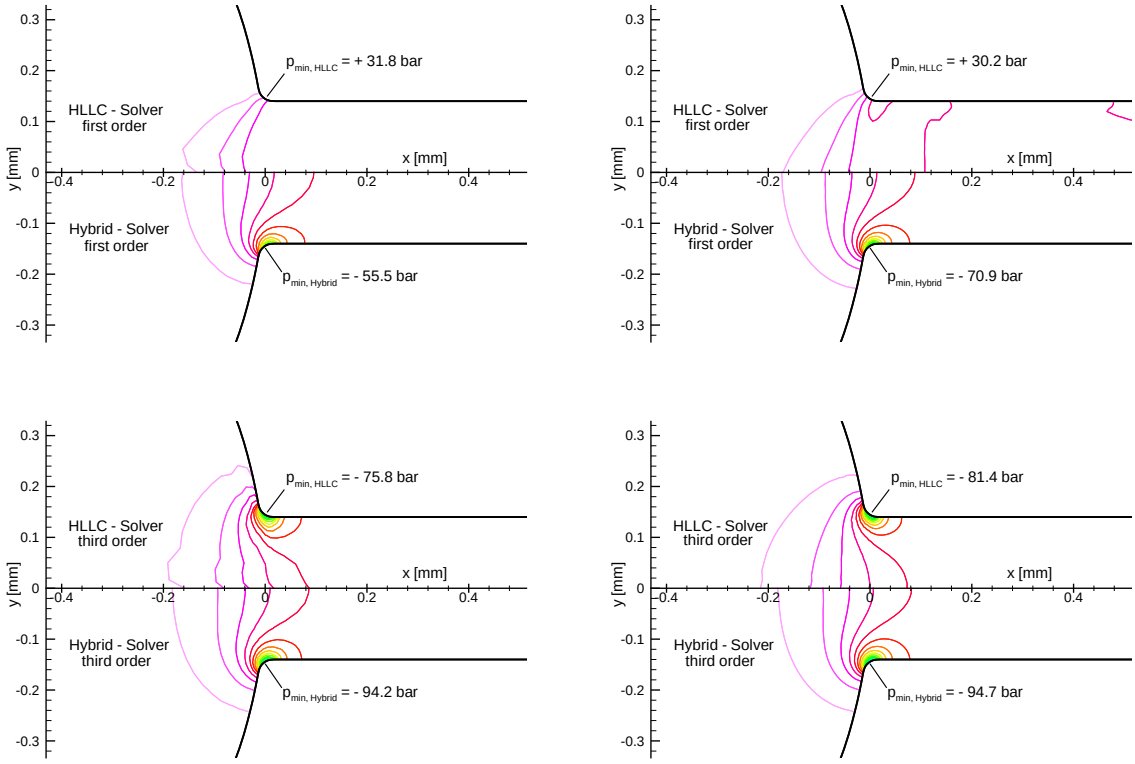

Figure 5: Comparison of HLLC (upper half) and Hybrid scheme (lower half) on the coarse grid (left) and on the fine grid (right) for the 2-D plane geometry.

we calculate the velocity at the outlet by using the given boundary conditions together with the area relation by evaluating the incompressible steady Bernoulli equation. For the given conditions we find an exit velocity of $u_{exit,Bernoulli} \approx 105\ m/s$. The first order HLLC scheme produces a steady-state result with an exit velocity of less then 50 m/s on the coarse grid and 64 m/s on the fine grid. This confirms the failure of the first order HLLC scheme on both grids. The pressure field as well as the velocity field (not shown) indicate a massively dissipating behavior of the HLLC solver for these flow conditions. For the third order simulations we find the same insufficiency, but the obtained solutions are more reasonable. The Hybrid scheme reproduced the analytical results very satisfactory

for all test cases. The gain in accuracy by using finer grids or higher order reconstructions is still noticeable, but a comparison of the isobars clearly shows that the main flow field is well predicted even for the first order solution on the coarse grid. We therefore conclude that our Hybrid formulation is a significant improvement.

5.4 3-D cavitating injection nozzles

To get more insight into the flow features in high-speed injection nozzles we have simulated a typical 3-D axisymmetric configuration with representative conditions (config 1). Additionally, we have modified the standard geometry by closing the axial inlet and adding four nearly tangential inlets in order to study swirl effects (config 2). This inlet configuration is then comparable to a mixing chamber. Both geometries are shown in Fig. 6. The nozzle dimensions are the same as for the previously presented 2-D single phase simulations (Fig. 4), but we added an outflow domain to study the wave dynamics outside the nozzle as well. Thereby, the whole domain is assumed to be initially filled with water at rest and pressure and temperature are assumed to be $p = 23\ bar$ and $T = 293.15\ K$. The conditions at the outflow boundaries are calculated by assuming that the farfield can

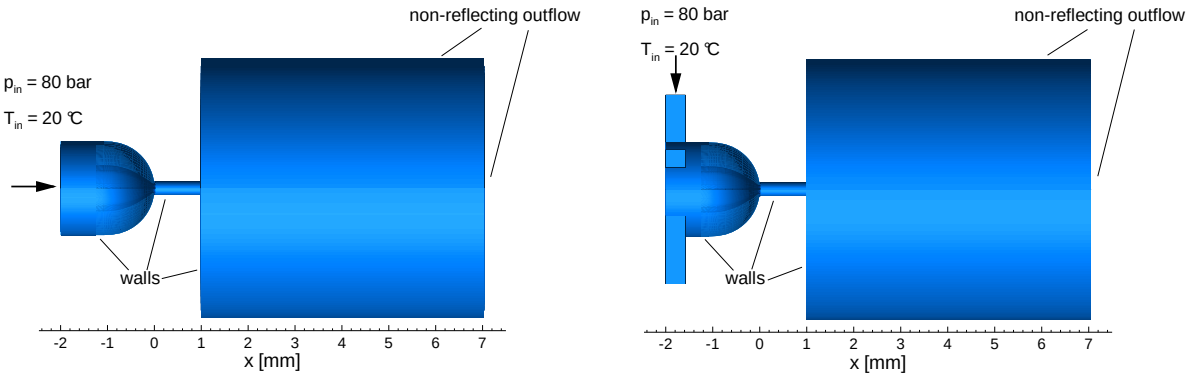

Figure 6: 3-D nozzle geometry with outflow and boundary definitions for nozzle configuration 1 (left) and configuration 2 (right)

be represented here by a liquid at rest (Fig. 6) with constant ambient pressure $p = 23\ bar$. According to these assumptions we derived characteristic boundary conditions that allow waves to pass through the boundary with minimum reflective behavior (non-reflecting boundary conditions). The walls are again defined as inviscid adiabatic and impermeable surfaces. The pressure for the ghost cells at the inlet plane was set to $p = 80\ bar$. The spatial reconstruction uses MinMod on density, WENO-3 on the velocities and VanLeer on internal energy. For the time integration the LS-RK 4 with $CFL = 1.3$ was used. To reduce calculation time, a 90 degree section of each full geometry was simulated. The

additionally resulting boundaries are treated with periodic conditions. Inside the nozzle we used a grid comparable to the coarse grid in Fig. 4. The total number of finite volumes for both geometries is $6 \cdot 10^4$ volumes per section and hence parameter studies are possible. For single-phase flows the grid was verified to be fine enough by comparing the numerical solutions with the Bernoulli theory. Nevertheless, we observed that a finer grid can lead to an increase in the resolved two-phase flow structures. The obtained flow fields for both configurations were found to be unconditionally time-dependent although the remaining variations are noticeably weaker then those during the buildup of the main flow fields. In Fig. 7 the iso-surfaces of constant vapor volume fraction α for configuration 1 are shown. The instantaneous picture gives an impression of the mean cavity length and the structure of the mixture region. Furthermore one can see two small cloudy structures that have been separated and convected into the outflow domain. The collapse of such structures can cause pressure waves of high amplitude with $\Delta p = \mathcal{O}(100)\ bar$. The second geometry

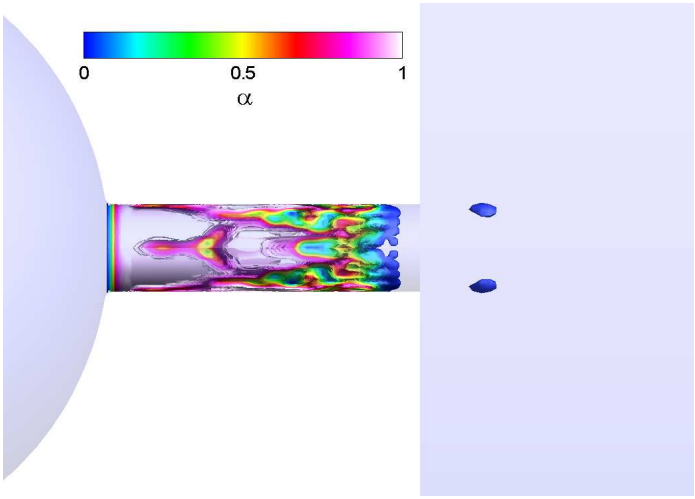

Figure 7: Iso-surfaces of the vapor volume fraction α at one instant in time for configuration 1

produces a more steady flow field because the inlet modification leads to the formation of a vortex structure. Only at the end of the cavitation core one can observe the separation of small cloudy structures. This breakup is periodic with a frequency $f = 60\ kHz$ and a series of planar cuts through the nozzle center is shown in Fig. 8. The flow inside the nozzle is nearly stationary and hence the use of a scheme that ensures accurate 3-D steady-state calculations is necessary for applications of this type[26]. To give an overall impression of the velocity field we generated stream traces starting from the inlets and ending at the outflow exit (Fig. 9). One can observe the acceleration in the convergent nozzle part and the rotational symmetric vapor core is visible (blue core).

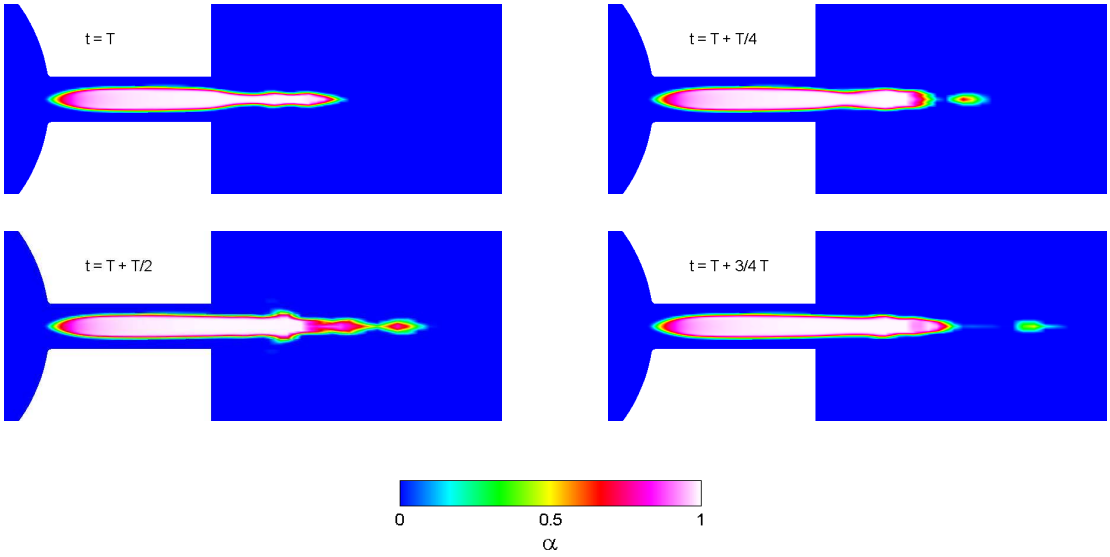

Figure 8: Vapor fraction α in configuration 2 for one period $T = 1/f = 1.7 \cdot 10^{-5}\ s$.

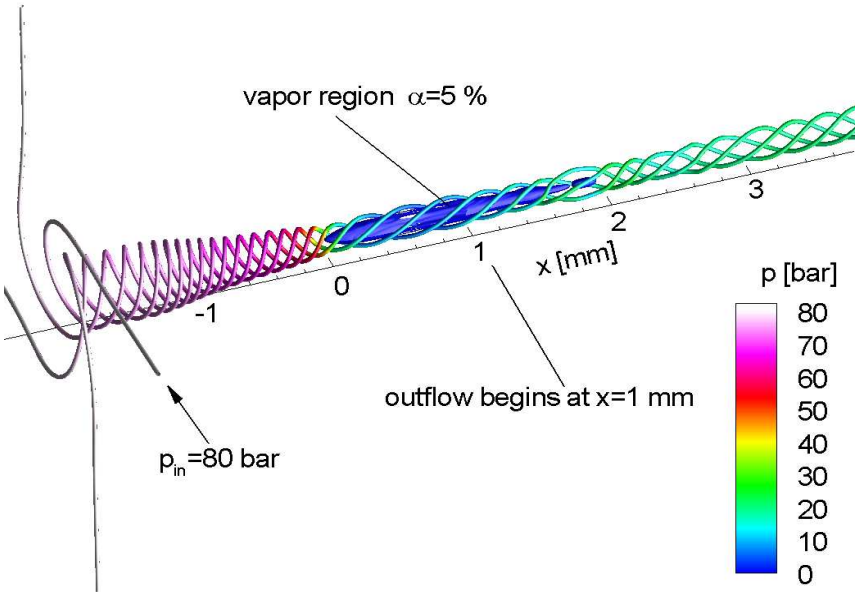

Figure 9: Stream traces at $t = T + T/2$ colored with the static pressure for configuration 2

6 CONCLUSIONS

- A general framework for solving the time dependent compressible Euler equations including the energy conservation law has been developed.
- An applicable set of constitutive relations for water and water vapor is given and their advantages as well as their disadvantages are described.
- It has been shown that accurate calculations of steady-state liquid flows require very fine grids and high-order reconstructions if common Riemann solvers are used.
- A Hybrid solver has been developed that overcomes the drawback of the previously stated approaches.
- The scheme was then shown to be able to handle two phase flow including the crucial phase change.
- Finally the cavitating flow fields through two different high-speed injection nozzles were presented.
- The present scheme should be extended to handle an additional gas component. This is especially important because it offers the possibility to simulate the outflow into a gaseous domain rather than a liquid one.

7 APPENDIX

For the simulations presented in section 6 the following set of constants and functions was used:

B	C_{v_l} $[kJ/(kgK)]$	T_{ref} $[K]$	$e_{l_{ref}}$ $[kJ/(kgK)]$	N
$3.3 \cdot 10^8$	4.18	273.15	0.617	7.15

Table 1: Constants for the liquid water EOS

R $[kJ/(kgK)]$	C_{v_v} $[kJ/(kgK)]$	T_{ref} $[K]$	$e_{l_{ref}}$ $[kJ/(kgK)]$	$L_{v_{ref}}$ $[kJ/(kgK)]$	κ
0.4615	1.4108	273.15	0.617	2375.3	1.327

Table 2: Constants for the water vapor EOS

The saturation conditions $p_{sat}(T)$, $\rho_{l,sat}(T)$ and $\rho_{v,sat}(T)$ are taken from[10]. If the temperature T is known to remain close to some reference value T_r, one can obtain approximations to the above cited functions which are more efficient to handle. The following example gives approximate conditions for a reference temperature $T_r = 293.15\ K$:

$$\theta := T - T_r \tag{28}$$

$$\begin{aligned} p_{sat}(T) &= exp(7.7585 + 0.0619166 \cdot \theta - 0.0002 \cdot \theta^2) \\ \rho_{l,sat}(T) &= exp(6.90591 - 0.00021 \cdot \theta - 0.000006 \cdot \theta^2 + 4.4 \cdot 10^{-8} \cdot \theta^3) \\ \rho_{v,sat}(T) &= exp(-4.05567 + 0.0585739 \cdot \theta - 0.000195 \cdot \theta^2) \end{aligned} \tag{29}$$

REFERENCES

[1] A. Berg, U. Iben, A. Meister, J. Schmidt. Modeling and simulation of cavitation in hydraulic pipelines based on the thermodynamic and caloric properties of liquid and steam. *Shock Waves*, (2005).

[2] C.E. Brennen. *Cavitation and Bubble Dynamics*, Oxford University Press, (1995).

[3] G.H. Schnerr. Modeling of unsteady cavitating flows - Status and future developments. *6th Int. Sym. on Experimental and Computational Aerothermodynamics of Internal Flows*, Shanghai, China, (2003).

[4] R. Saurel, J.P. Cocchi and P.B. Butler. Numerical study of cavitation in the wake of a hypervelocity underwater projectile. *Journal of Propulsion and Power*, **15**, 4, (1999).

[5] C. Hirsch. *Numerical Computation of Internal and External Flows*, John Wiley & Sons, Vol. 1-2, (1988).

[6] A. Harten, P.D. Lax, C.D. Levermore and W.J. Morokoff. Convex entropies and hyperbolicity for general Euler equations. *SIAM J. Numer. Anal.*, **35**, 6, 2117–2127, (1998).

[7] M.J. Ivings, D.M. Causon and E.F. Toro. On Riemann solvers for compressible liquids. *Int. J. Numer. Meth. Fluids*, **28**, 395–418, (1998).

[8] P.A. Thompson. *Compressible Fluid Dynamics*, McGraw Hill, (1972).

[9] J.O. Hirschfelder, C.F. Curtiss and R.B. Bird. *Molecular Theory of Gases and Liquids*, John Wiley & Sons, (1965).

[10] R. Oldenbourg. *Properties of Water and Steam in SI-Units*, Springer-Verlag, (1989).

[11] G. Benedetto, R.M. Gavioso, P.A.G. Albo, S. Lago, D.M. Ripa and R. Spagnolo. Speed of sound of pure water at temperatures between 274 and 394 K and pressures up to 90 MPa. *Fifteenth Symposium on Thermophysical Properties*, Boulder, Colorado, U.S.A., (2003).

[12] W. Wallis. *One Dimensional Two-Phase Flow*, McGraw Hill, (1975).

[13] The International Association for the Properties of Water and Steam, *http://www.iapws.org/*.

[14] R.B. Eddington. Investigation of supersonic phenomena in a two-phase (liquid-gas) tunnel. *AIAA Journal*, **8**, 1, (1970).

[15] W. Wagner, S. Span and T. Bonsen. *Wasser und Wasserdampf*, Electronic Media, Springer-Verlag, (1999).

[16] S.K. Godunov. A finite difference method for the numerical computation of discontinuous solutions of the equations of fluid dynamics. *Mat. Sb.*, **47**, (1959).

[17] E.F. Toro. *Riemann Solvers and Numerical Methods for Fluid Dynamics*, Springer-Verlag, (1999).

[18] T.J. Chen and H. Cooke. On the Riemann problem for liquid or gas-liquid media. *International Journal for Numerical Methods in Fluids*, **18**, 529–541, (1994).

[19] R. Menikoff, B.J. Plohr. The Riemann problem for fluid flow of real materials. *Reviews of Modern Physics*, **61**, 1, (1989).

[20] P. Colonna and S. Rebay, Numerical simulation of dense gas flows on unstructured grids with an implicit high resolution upwind Euler solver, *Int. J. Numer. Meth. Fluids*, **46**, 7, pp. 735-765, (2004).

[21] E. Turkel. Preconditioning techniques in fluid dynamics. *Annual Review of Fluid Mechanics*, **31**, (1999).

[22] A. Meister. Asymptotic single and multiple scale expansions in the low Mach number Limit. *SIAM J. Appl. Math.*, **60**, 1, 256–271 (1999).

[23] H. Guillard and C. Viozat. On the behaviour of upwind schemes in the low Mach number limit. *Computers & Fluids*, **28**, 66–86 (1999).

[24] M.S. Liou. A sequel to AUSM, part II: AUSM+ -up for all speeds. *Journal of Computational Physics*, **214**, 137–170, (2006).

[25] M.S. Liou and C.J. Steffen. A new flux splitting scheme. *Journal of Computational Physics*, **107**, 23–39, (1993).

[26] S.J. Schmidt, I.H. Sezal and G.H. Schnerr. On Godunov methods for liquid flows. to be published.

[27] R.J. Leveque. *Finite Volume Methods for Hyperbolic Problems*, Cambridge University Press, (2002).

[28] C.W. Shu. Essentially non-oscillatory and weighted essentially non-oscillatory schemes for hyperbolic conservation laws. *ICASE Report No. 97-65*

[29] S. Gottlieb and C.W. Shu. Total variation diminishing Runge-Kutta schemes. *Mathematics of Computation*, **67**, 221, (1998).